

Direct Imaging of Carbon Nanotube Liquid-Crystalline Phase Development in True Solutions

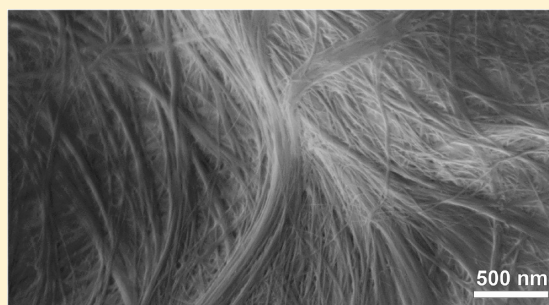
Olga Kleinerman,^{†,§} Lucy Liberman,^{†,§} Natnael Behabtu,[‡] Matteo Pasquali,^{*,‡} Yachin Cohen,[†] and Yeshayahu Talmon^{*,†}

[†]Department of Chemical Engineering and the Russell Berrie Nanotechnology Institute (RBNI), Technion - Israel Institute of Technology, Haifa 3200003, Israel

[‡]Department of Chemical & Biomolecular Engineering, Department of Chemistry, Department of Materials Science & NanoEngineering, and the Smalley-Curl Institute, Rice University, 6100 Main Street, Houston, Texas 77005, United States

Supporting Information

ABSTRACT: Using direct-imaging cryogenic transmission and scanning electron microscopy, we show different stages of liquid-crystalline phase development in progressively more concentrated solutions of carbon nanotubes in chlorosulfonic acid: a dilute phase of individually dissolved carbon nanotubes; semidilute and concentrated isotropic phases; coexisting concentrated isotropic and nematic phases in local equilibrium with each other; and a fully liquid-crystalline phase. Nanometric resolution of cryogenic electron microscopy reveals carbon nanotube self-assembly into liquid-crystalline domains of several nanometers in width at very early stages. We find significant differences in carbon nanotube liquid-crystalline domain morphology as a function of the carbon nanotube aspect ratio, diameter, and degree of purity.



■ INTRODUCTION

A repeating covalently bonded unit of carbon atoms characterizes the individual carbon nanotube (CNT) structure.¹ Taking into account the organic nature of CNT, with a high aspect ratio and a relatively low density, there is a strong parallel between a single CNT molecule and a conventional rigid polymer.² In fact, such a parallel between CNTs and polymers was first suggested in 1999 by Shaffer and Windle,³ although it could not be demonstrated experimentally at that time because early CNT samples had poorly controlled and inadequately characterized structure, and no solvents had yet been found for this class of materials.^{4,5} Starting in the mid-2000s, evidence started accumulating on the dissolution of CNTs in strong acids,^{6,7} leading to our demonstration that CNTs spontaneously dissolve in chlorosulfonic acid (CSA),⁸ with solubility being controlled by the acid strength and CNT diameter⁹ as long as the CNTs have a low defect density.¹⁰ CSA and other strong acids act as thermodynamic solvents by protonating CNT sidewalls and causing a repulsion that counteracts the van der Waals attractive forces between CNTs.^{6,11} At sufficiently high concentration, CNTs in strong acids form liquid-crystalline phases,^{7,8} from which macroscopic, continuous CNT fibers can be spun.^{12,13} Much like in earlier examples in the rigid-rod polymer fiber literature,^{14,15} fiber spinning from a liquid-crystalline state is essential to attaining a high degree of CNT orientation and packing in fibers, thus translating the intrinsic unique properties of the individual CNT molecule in the macroscopic fiber.¹² These novel materials display a unique combination of strength, flexibility, and electrical and thermal

conductivity;¹² therefore, understanding the basic science that lies at the foundation of their processing is critical for further progress toward the development and deployment of CNT material technology.¹⁶

Unlike earlier rigid-rod polymers, which include well-defined single molecular species, macroscopic CNT samples always include a range of molecules with chemical (in addition to physical) polydispersity;¹⁷ their phase behavior depends on the CNT type, defect concentration, CNT length, and acid solvent strength.^{8,10} Moreover, CNT solutions have extreme values of key polymeric features, whereas both the length and persistence length of CNTs are about 100 to 10 000 times higher than for rigid rod polymers. Individual CNT properties such as diameter and length can be determined via TEM¹⁸ and shear and extensional rheology.^{19,20} The persistence length (a measure of molecular stiffness) is known to grow with CNT diameter.²¹ Raman spectroscopy can be used to measure the degree of protonation of the CNTs in acidic solvents,^{6,8} thereby providing a measure of solvent strength for each pair of CNTs and acids. However, none of these techniques provides insight into CNT phase morphology. The X-ray scattering of CNTs in acids is made difficult by the large scattering cross section of sulfur, which dominates the signal from the carbon.^{22,23} Polarized light microscopy (PLM) allows direct imaging of CNT solutions and thus is most useful for

Received: February 16, 2017

Revised: April 4, 2017

Published: April 4, 2017

determining the onset of a liquid-crystalline phase as well as some coarse morphological features of the LC phase.^{8,10,19,24–26} However, PLM has limited resolution (\sim micrometer size). Because of these limitations, PLM can image only coarse information on long-range CNT ordering and cannot reveal how CNTs pack, orient, and perhaps deform within LC domains or how LC domains merge into each other. Moreover, PLM cannot show how concentration fluctuations may lead to the formation of an LC phase. Cryogenic electron microscopy (cryo-EM) is the highest-resolution tool for imaging the nanostructure of liquid systems; it has been used in the literature to study systems of rodlike molecules,²⁷ although sample preparation artifacts have prevented an accurate study of phase behavior in the past. The first cryogenic transmission electron microscopy (cryo-TEM) images of a CNT dispersion were published by Bandyopadhyaya et al.,²⁸ a decade after CNT discovery. Since then, the number of reports using cryo-TEM as a characterization tool for CNT dispersions has been growing steadily. Most of the CNT dispersions analyzed by cryo-TEM are dilute surfactant-stabilized aqueous suspensions.^{29,30} We have overcome the difficulties of preparing and imaging acid solvents by the development of unique cryo-EM specimen preparation and imaging methodologies. In an earlier publication, we described the methodology and demonstrated its application in the study of the CNT-CSA system.³¹ Here, we present a systematic study of the entire range of liquid-crystalline phase development and its nanoscale arrangement in CNT-CSA solutions by direct cryo-EM imaging, starting from dilute solutions up to concentrated liquid-crystalline CNT phases used as the “dope” for fiber spinning. We analyze several types of CNTs that differ by their length-to-diameter (L/D) ratio (or aspect ratio), diameter, number of walls, degree of purification, and structural defects and study their relation to the phase-transition path. We reveal the morphology of nascent liquid-crystalline domains at concentrations just above the isotropic cloud point and the defect structure in the high-concentration liquid-crystalline phase. This work is the first direct imaging of CNT solutions (and most probably of any LC system) across the whole phase diagram, within the conceptual framework first laid out by Onsager and Flory.^{32,33}

EXPERIMENTAL SECTION

High-purity single-walled carbon nanotubes (SWNTs) were obtained from the high-pressure carbon monoxide reactor (HiPco) at Rice University. Double-walled carbon nanotubes (DWNT) were purchased from Carbon Nanotechnologies, Inc. (CCNI) and Teijin Aramid BV (AC299). CNTs were used as received, except for the AC299 grade, which was purified at Rice University (marked as AC299p). ACS-certified chlorosulfonic acid (CSA) was used as received from Sigma-Aldrich (St. Louis, MO). CNTs were dispersed in CSA at several concentrations, up to 6 wt %, without any additional treatment or sonication. The solution preparation procedure is described in detail elsewhere.^{8,31} Low-viscosity specimens were examined with a Philips CM120 or an FEI Tecnai 12 G² transmission electron microscope at an accelerating voltage of 120 kV in the low-dose imaging mode. We used a Gatan 626 cryo-holder to maintain the vitrified specimens below -175 °C. Images were recorded digitally with a Gatan MultiScan 791 cooled CCD camera (Philips microscope) or with a $2k \times 2k$ Gatan US1000 cooled CCD camera using Digital Micrograph software (Gatan, U.K.). High-viscosity specimens, which could not be thinned into a thin film, were examined in a Zeiss Ultra Plus high-resolution scanning electron microscope (HR-SEM) at cryogenic temperature. The microscope is equipped with a BalTec (now Leica) VT100 cold-stage system. Cryo-SEM specimens were maintained at -145 °C for high-resolution imaging. We used a low

electron acceleration voltage (0.7 to 2 kV), short working distance (2.9–3.3 mm), and InLens secondary electron detector, in some cases combined with an Everhart-Thornley detector. The cryo-EM specimen preparation procedure for the direct imaging of highly acidic systems is a multistep technique that was developed and described in detail by Kleiner et al.³¹

Wide-angle X-ray diffraction of single CNT fibers was performed on a small-/wide-angle diffractometer (Molecular Metrology SAXS system) equipped with a sealed microfocus tube (MicroMax-002+S) emitting Cu $K\alpha$ radiation ($\lambda = 1.542$ Å), two Göbel mirrors, and three pinhole slits. The generator was powered at 45 kV and 0.9 mA. The scattering patterns were recorded with a 15×15 cm² two-dimensional imaging plate (BAS-IP-MS, Fujifilm), positioned about 2.8 cm behind the sample. The scattering intensity was recorded over the interval of $0.21 < Q < 4.5$ Å⁻¹, where Q is the scattering vector. The exposure time was 30–120 min. The single-fiber sample (diameter ~ 10 – 20 μ m) was fixed on a two-dimensional holder perpendicular to the beam and measured under vacuum at ambient temperature. The imaging plate was scanned with a fluorescent image analyzing system (FLA-7000) and analyzed with FLA-7000 ImageReader software (version 10) with 100 μ m resolution.

RESULTS AND DISCUSSION

We investigated several types of CNTs in CSA at different concentrations, probing the entire spectrum of phase behavior from the dilute phase through the isotropic, biphasic, and, finally, the fully liquid-crystalline regime. Table 1 summarizes the CNT parameters and phase-transition concentration by weight (w_{iso}).^{19,34}

Table 1. Average Physical Parameters of CNTs in the Current Study

CNT batch	number of walls ^a	W_{iso} (ppm) ^b	diameter (nm) ^a	aspect ratio (L/D) ^c
HiPco 187.5	1	1400	1	550
CCNI 1001	2	175	1.9	2500
CCNI 1101	2.6	150	3.2	2800
CCNI 1002	2	90	2	3000
AC299p	2	40	2	9600

^aThe number of walls and diameter were quantified by high-resolution transmission microscopy (HR-TEM). ^bThe isotropic-to-nematic phase transition concentration by the weight (w_{iso}) of each CNT type was determined by polarized light microscopy. ^cThe CNT length was measured by extensional rheology¹⁹ and by a statistical method applied to cryo-TEM images.¹⁸

In general, the phase behavior in solutions or suspensions of rodlike molecules can be understood in terms of progressively more concentrated regimes, where different rod–rod interactions are important,³⁵ as schematically depicted in Figure 1 (top). At low enough concentration, rods are termed dilute because they do not interact with each other (other than by long-range hydrodynamic interactions). In the semidilute regime, rods sterically confine each others' rotational diffusion. As the concentration increases further, the concentrated isotropic regime is reached, where both rotational and translation diffusion are restricted by mutual steric hindrances.

Beyond a critical concentration, the concentrated isotropic phase becomes unstable, and a spontaneously aligned liquid-crystalline phase forms as the rod gives up rotational entropy to gain translational entropy due to the excluded volume. In a certain range of concentrations, the concentrated isotropic phase coexists with a liquid-crystalline phase prior to the formation of single-phase liquid crystal at sufficiently high

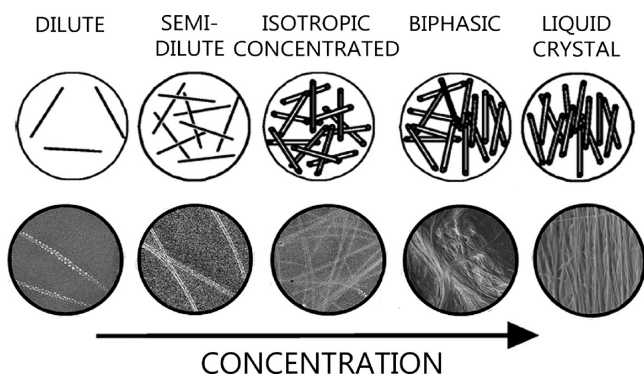


Figure 1. (Upper panel) Model of aligned phase development in an athermal rigid-rod polymer solution, as predicted by Flory's model in 1956³³ and schematically presented by Doi and Edwards in 1986.³⁵ The concentration of solute is increased from left to right. (Lower panel) Cryo-EM micrographs, showing liquid-crystalline phase development in CNT/CSA solution as a function of nanotube concentration (this work). Dilute, semidilute, and isotropic phases are cryo-TEM micrographs. Biphasic and fully liquid-crystalline phases are cryo-SEM images.

concentration.^{32,33} In the biphasic region, the proportion of the aligned phase grows with rod concentration. The width of the biphasic region depends on the rod polydispersity and solvent quality (higher polydispersity and weaker solvents yield broader biphasic regions). Figure 1 (bottom) shows the first direct imaging of the progression of the fluid nanoscale structure as the concentration is increased from a few ppm to several percent by weight (tens of hundreds of ppm), and the system transitions from dilute, through the semidilute and concentrated isotropic phases, all the way to a full liquid crystal. These phase transitions and morphologies are discussed extensively in the following sections.

Liquid-Crystalline Phase Formation. Figure 2 gives a series of cryo-TEM images that display the typical liquid-crystalline phase formation stages, observed in all types of CNTs used in the current study, regardless of their parameters (Table 1). At low concentration (~20 ppm), the CNTs are dispersed individually (arrowheads in Figure 2a), although typically we find that CNTs at this concentration already intersect in the images, indicating that the solution may already be semidilute (or that the CNTs came into near contact during the process of blotting that thins the liquid film to ~100 nm and therefore confines the long CNTs to a nearly 2D plane). The bright cavities around the CNTs seen on the dark background of vitrified CSA are the result of electron beam radiation damage at the CNT/CSA interface.³¹ As the concentration increases, the CNTs form a loose isotropic network (arrowheads in Figure 2b). At higher CNT concentration, the isotropic–nematic phase separation is observed in its early stages (Figure 2c). Narrow aligned domains, 15–50 nm wide (arrows in Figure 2c), coexist with more extended areas of a concentrated isotropic phase. By doubling the CNT concentration, larger areas (>100 nm, arrows in Figure 2d) of locally aligned CNTs are observed, coexisting with thinner ones. As the CNT concentration increases further, a shorter exposure time (i.e., a lower electron dose) is needed to obtain sufficient contrast between the CNTs and the acid. As a result, radiation damage of the more concentrated solutions is significantly reduced in the images we show here. In addition to its importance in fundamental phase

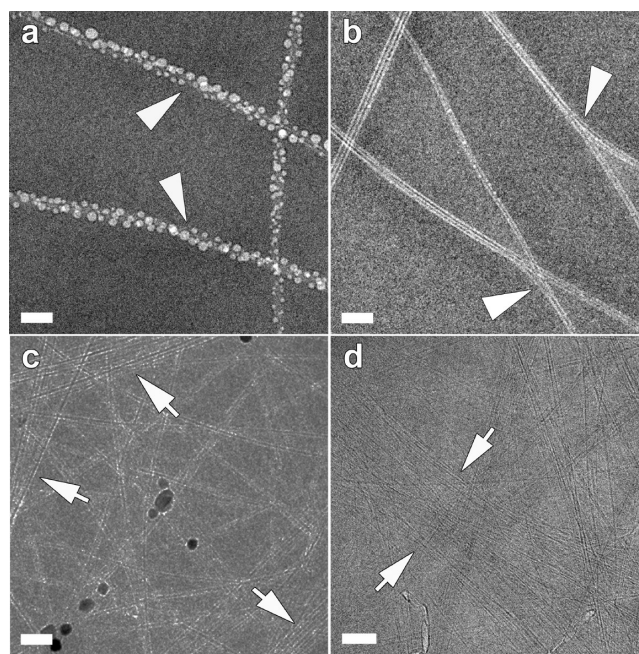


Figure 2. Cryo-TEM micrographs of CNT/CSA solutions (CCNI 1101 DWNTs, $w_{\text{iso}} = 150$ ppm by weight) showing liquid-crystalline phase development as a function of nanotube concentration: (a) 20, (b) 75, (c) 100, and (d) 250 ppm by weight. In (a), we see long nanotubes are dissolved as individuals (white arrowheads). As the concentration increases, CNTs overlap, forming a semidilute isotropic phase. In (c), the initial stage of nematic phase formation is observed (arrows) on the background of the concentrated isotropic phase. Black spots in (c) are crystalline ice contamination. Micrograph (d) shows wider CNT nematic domains (arrows) with a much lower isotropic phase content. Scale bars are 50 nm.

behavior studies, the perfect dispersion of CNTs in CSA in the dilute and semidilute regimes can be used to measure the CNT length by postprocessing of cryo-TEM micrographs¹⁸ as well as using extensional rheology.¹⁹

The biphasic region is particularly interesting because recent studies on actin found a change from first order to a continuous isotropic–nematic transition as actin filaments grew longer.^{36,37} We have extensively studied the intermediate biphasic region, especially near the isotropic-to-biphasic boundary for different types of CNTs. Working with different CNT samples, we noticed that LC phase formation is accompanied by the segregation of defective or irregular CNTs and impurities out of the ordered phase. This phenomenon was noticed by Zhang during an inspection of dried LC samples;³⁸ for the first time, it is highlighted here by direct imaging of CNT solutions. Figure 3 shows isotropic (Figure 3a) and nematic (Figure 3b) phase coexistence in the same solution of long CNTs (CCNI 1002) at a concentration of 570 ppm by weight. In this particular sample, we observed many carbon impurities and damaged CNTs in comparison to other studied CNTs. Distorted CNTs filled with acid are seen, as well as empty ones, having irregular shapes (arrowheads in Figure 3a). Such CNTs are segregated into the isotropic phase (Figure 3a), whereas aligned domains consist mostly of undamaged uniform CNTs (Figure 3b). If the isotropic and LC phases could be separated effectively, then the absence of defective CNTs from the LC phase could be used as a tool to purify CNT samples of defective CNTs.

Aspect Ratio Effect. The supramolecular resolution of cryo-TEM allowed us to capture the structure close to the

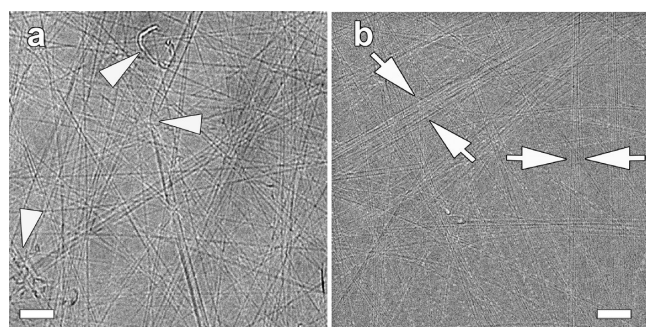


Figure 3. Cryo-TEM images of CCNI 1002 in CSA, 570 ppm by weight, showing the coexistence of an (a) isotropic and (b) a nematic liquid-crystalline phase in the same sample. Measured w_{iso} of CCNI 1002 is about 90 ppm by weight. Aligned CNT domains consist of molecules with similar diameter (arrows in (b)), and the impurities and different molecules are segregated out of the aligned phase (arrowheads in (a)). Scale bars are 50 nm.

isotropic-to-nematic phase-transition boundary and to compare the morphology differences at the concentrated isotropic-to-biphasic phase boundary for long and short CNTs (Figure 4a,b). This figure represents the concentrated isotropic phase of

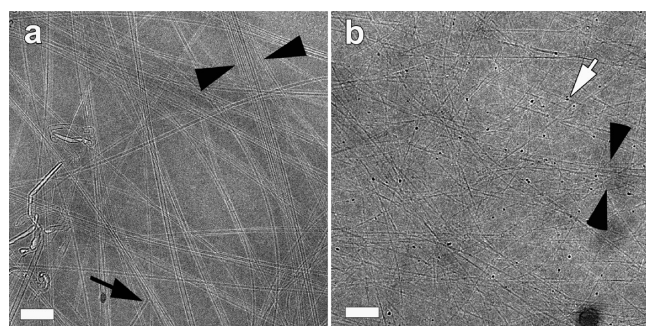


Figure 4. Cryo-TEM images of (a) CCNI 1002 DWNTs in CSA, 10 ppm by weight, and (b) HiPco 187.5 SWNTs, 250 ppm by weight. Both types show a concentrated isotropic phase close to the isotropic/biphasic boundary. An arrow in (a) points to a bent CNT filled with acid. An arrow in (b) indicates a catalyst particle. In both images, black arrowheads show LC domains in an early stage of formation. Scale bars are 50 nm.

long CCNI 1002 CNTs with a mean diameter of 2 nm, $L/D \approx 3000$, compared to the concentrated isotropic phase of short HiPco 187.5, 1 nm diameter, $L/D \approx 550$ CNTs. Damaged and irregular CNTs cause local distortions in the network (arrow in Figure 4a). The very onset of liquid-crystalline phase formation can also be observed (arrowheads in Figure 4a,b). In HiPco samples, defective CNTs are hard to recognize because of the very small CNT diameter. Seemingly, the effect of small damaged CNTs on the isotropic phase morphology is minor.

The phase-transition concentration (or the so-called isotropic cloud point, w_{iso}) of CNT solutions varies with CNT properties, such as diameter, aspect ratio (L/D), and degree of purity. Extensional rheology of different CNT batches showed a linear dependence of w_{iso} with respect to the aspect ratio,¹⁹ following the general $(L/D)^{-1}$ dependence predicted by Flory and Onsager. Our cryo-TEM analysis of CNTs with different aspect ratios showed the same trend: for longer CNTs, w_{iso} is tens of ppm by weight, whereas for shorter CNTs w_{iso} rises to thousands of ppm by weight. For the CNTs shown in

Figure 5, the isotropic-to-nematic transition occurs around 1400 ppm by weight for short HiPco 187.5 CNTs and at 40

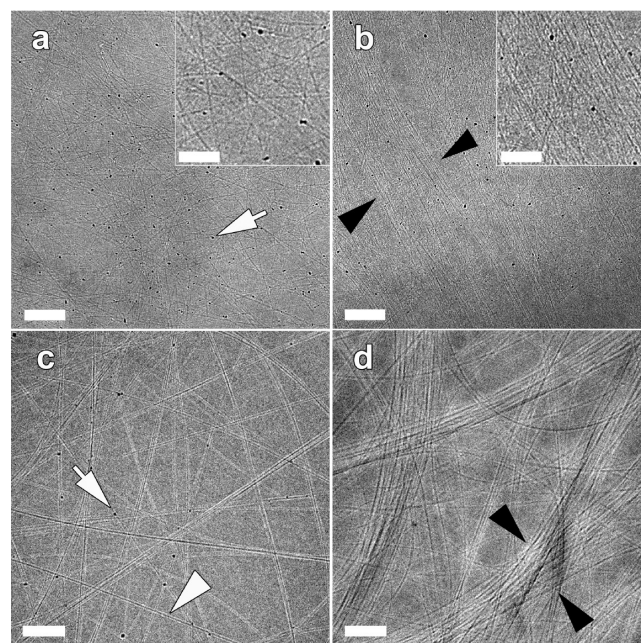


Figure 5. Cryo-TEM images of CNT/CSA solution showing the isotropic-to-biphasic phase transition and morphology as a function of the nanotube aspect ratio. (a) Isotropic phase of short HiPco 187.5 SWNTs, 250 ppm by weight ($L/D = 550$, $w_{\text{iso}} \approx 1400$ ppm). (b) Biphasic region of HiPco 187.5, 2500 ppm by weight. (c) Concentrated isotropic phase of long AC299p, 20 ppm by weight ($L/D = 9600$, $w_{\text{iso}} \approx 40$ ppm). (d) Biphasic region of AC299p, 200 ppm by weight. White arrows in (a) and (c) point to catalyst particles. The arrowhead in (c) shows radiation damage along a CNT wall. Arrowheads in images (b) and (d) enclose LC domains. Scale bars are 100 nm. Insets in (a) and (b) are enlarged views of the CNT arrangement in isotropic and liquid-crystalline phases. Scale bars are 50 nm.

ppm by weight for AC299p long CNTs (Table 1). Figure 5a,c represents isotropic networks of short and long CNTs at concentrations of 250 and 20 ppm by weight, respectively. Nanostructures in the biphasic regime of the same CNTs are shown in Figure 5b (short HiPco) and Figure 5d (long AC299p). At higher CNT concentrations, narrow ordered domains consisting of long, straight CNTs parallel to each other are observed. In the nematic domains of shorter CNTs (Figure 5b), adjacent CNTs are less aligned than in the case of longer CNTs (Figure 5d). The liquid-crystalline domain of longer CNTs, shown in Figure 5d, also appears to be more compact than that of the shorter CNTs (Figure 5b). The appearance of LC domains with a spacing between adjacent long CNTs, on the order of a few diameters, was modeled by Green et al.¹¹ as being due to the attractive potential between adjacent CNTs, being more prominent at increasing length. The imaged coexisting isotropic and nematic domains are in local equilibrium and do not reflect global thermodynamic equilibrium because the surface between the two phases is not minimized. The nematic domains may be precursors to larger-scale tactoid structures that have been visualized in the CNT–acid system³⁹ and can exist as long-lived structures, as described in recent theories.^{40,41} The CNT packing described above in the liquid-crystalline solution should strongly affect the

macroscopic bulk properties of the dope (such as the rheological behavior) and the fibers spun from it.

Biphasic Region. As the CNT concentration shifts into the biphasic region, thin aligned domains merge into thicker ones to produce a network in a crisscross manner, as shown in Figure 6a. Interestingly, solid, thin CNT films dip-coated from

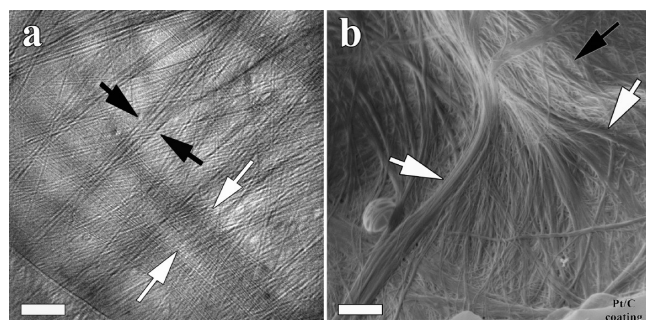


Figure 6. Cryo-EM images showing the development of a network of ordered CNT domains in the biphasic region of long CCNI 1001 DWNTs in CSA. (a) Cryo-TEM micrograph of 1000 ppm CNTs in CSA by weight and (b) cryo-SEM image of the same batch, 5000 ppm by weight in CSA. (a) Scale bar = 50 nm and (b) scale bar = 500 nm.

the low-concentration biphasic regime show a similar crisscross pattern of aligned CNT bundles.⁴² The process of liquid-crystalline domain networking increases the solution viscosity.⁷ Highly viscous solutions cannot be thinned down into a cryo-TEM film; therefore, with increasing CNT content toward the biphasic/nematic phase boundary in the same sample, we use cryogenic scanning electron microscopy (cryo-SEM) direct imaging. The cryo-SEM image in Figure 6b of CCNI 1001 CNTs shows elongated, randomly branched nematic domains of CNTs (white arrows) superposed on an isotropic phase background (black arrow). We note the possible influence of shear on the solution during cryo-TEM specimen preparation.

Polydispersity. Aspect ratio polydispersity is known to broaden the biphasic region because lower-aspect-ratio rods concentrate in the isotropic phase, whereas higher-aspect-ratio rods preferentially segregate into the nematic phase.^{2,43–45} In our samples, aspect ratio polydispersity is due to distributions in both the CNT diameter and length. Interestingly, Figure 6a shows spontaneous separation by diameter in nematic domains within a particular sample. An aligned domain of thinner CNTs is seen in between white arrows, and domains of thicker CNTs are between black arrows. Such images are typical of CNT batches with high-diameter polydispersity. Segregation by CNT diameter is not expected on the basis of excluded volume alone and may indicate the presence of diameter-specific CNT–CNT interactions in the acid solvent.

Effect of Impurities. A large amount of amorphous carbon and other CNT allotropes significantly decreases the CNTs surface area available for protonation. Indeed, solutions of purified material exhibit a better dispersion of individual CNTs in the solution, improving the homogeneity of the isotropic phase and increasing the CNT capacity in it. In addition, by lowering the impurity content in solution, a better packing of ordered domains is achieved. Thus, CNT purification increases the isotropic cloud point and narrows the biphasic region. CCNI 1002 and CCNI 1001 CNTs are good examples to highlight the purification effect on phase behavior. Both CNT types, CCNI 1002 and CCNI 1001, have similar aspect ratios. However, according to PLM, the phase-transition concen-

tration of CCNI 1002 is about 90 ppm by weight versus 175 ppm for CCNI 1001 (Table 1). Direct cryo-TEM imaging of both CNT batches showed that in CCNI 1002 the impurity content is much higher than in CCNI 1001, and phase separation of CCNI 1002 occurs at around 10–20 ppm (Figure 4a), an order of magnitude lower than what is expected. Such a shift could be explained by several reasons. Aligned domains at the very beginning of phase separation are about 50–200 nm wide and could not be visualized by PLM. Also, there is a possibility of a shear-induced phase transition during cryo-TEM specimen preparation, which reduces the apparent transition concentration shown by cryo-TEM as compared to that of PLM. However, this effect is consistent for all cryo-specimens; thus, it is reasonable to relate different w_{iso} values of similar CNT types to different degrees of purity. Visual observation of the effect of CNT structural defects on the phase transition concentration provides an additional aspect of rigid-rod molecule behavior in solution.

Liquid-Crystalline Phase. We also characterized a fully developed liquid-crystalline phase. Because these solutions are viscous, the imaging was carried out with cryo-SEM.³¹ This phase is used as a dope for fiber spinning.^{12,25} Figure 7 shows

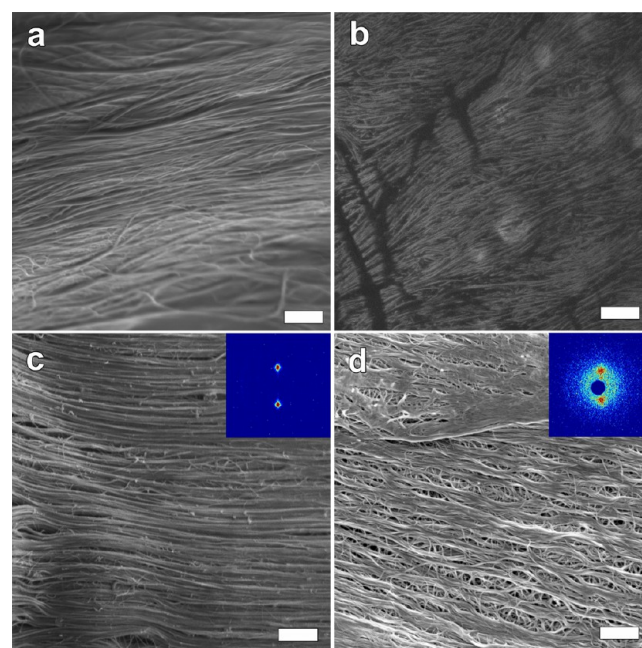


Figure 7. Cryo-SEM micrographs of the LC dope consisting of (a) long CCNI 1101 CNTs, 3% by weight in CSA and (b) short HiPco CNTs, 6% by weight in CSA. RT-SEM micrographs of a CNT fiber spun from an LC dope of (c) CCNI 1101 CNTs, 3% by weight. (d) HiPco CNTs, 4% by weight. The insets in (c) and (d) are wide-angle diffraction patterns from the same fibers. (Line scans are presented in the Supporting Information.) Scale bars are 500 nm.

the liquid-crystalline domains formed by CCNI 1101 with $L/D \approx 2800$ and by HiPco CNTs with $L/D \approx 550$ in CSA. The differences in the aspect ratio between the CNTs lead to full LC phase formation at a much lower solution concentration for CCNI 1101 as compared to that for HiPco.

Cryo-SEM micrographs reveal very different arrangements of these CNTs at the nanometric level. The longer CNTs form elongated aligned domains (Figure 7a), whereas the LC phase of shorter CNTs consists of smaller and less ordered domains (Figure 7b). This effect may be caused partially by shear during

cryo-SEM specimen preparation. Longer CNTs align under shear more readily than short ones, and there is not enough time for the system to relax prior to vitrification. Reduced or no specimen charging during SEM imaging was observed during the imaging of longer CNTs at higher concentration, which implies that CNTs continuously span the whole bulk sample, leading to improved electron conductivity. During SEM imaging, better conductors neutralize the sample surface from charge accumulation, preventing charging. Figure 7c,d shows HR-SEM images of CNT fibers, spun from the LC dope of CNT/CSA solutions, discussed above, via a wet spinning process. Small-diameter HiPco CNTs, which are much shorter than CCNI CNTs, exhibit less ordered structures on the fiber surface (Figure 7d) as compared to very long and thick CCNI CNTs (Figure 7a). These observations are consistent with the differences observed with the full LC phase behavior of long CCNI 1101 in contrast to that of HiPco in CSA dopes (Figure 7a,b, respectively). Although most HR-SEM images at ambient temperature showed the CNT arrangement on the fiber surface rather than its internal morphology, wide-angle X-ray diffraction (WAXD) experiments provided information regarding the entire fiber structure as a larger volume is sampled in a single experiment. By comparing simulated WAXD equatorial plots⁴⁶ with experimental results (Figure S1 in the Supporting Information), we assume that the most intense peak in the diffraction pattern corresponds to CNT packing into a hexagonal structure within the fiber. Whereas the WAXD pattern of a CCNI 1101 fiber shows sharp and localized reflections, an indication of a well-aligned crystalline structure with a Herman's orientation factor of 98.6% (inset in Figure 7c and Figure S2), the WAXD pattern of the HiPco CNT fiber is characterized by more diffuse reflections (inset in Figure 7d and Figure S3). The Herman's orientation factor for the HiPco fiber is 91.3%, indicating better alignment in fibers made of longer nanotubes. This observation is consistent with cryo-SEM imaging of the liquid-crystalline domains (Figure 7a,b) and SEM images of the fiber surface spun from these solutions (Figure 7c,d).

SUMMARY AND CONCLUSIONS

Direct imaging of CNT/CSA solutions provides a detailed view of the liquid-phase microstructure development and its influence on final material microstructure. There are significant differences in the formation of ordered domains of short and long CNTs from the very early stage, affecting the LC phase morphology of the dope and, as a result, that of the spun fibers. The combination of methods developed and applied to the characterization of CNT phase behavior, from dilute up to lyotropic liquid-crystalline phases, could serve as a routine technique for a better control in solution-based shaping techniques of high-performance CNT materials (fiber, films, membranes, and foams). In addition, we found that cryo-EM of CNT/CSA solutions in the native state proved to be a very useful tool for raw material quality assessment in terms of the purity, CNT size distribution, and presence of defects. The combination of cryo-TEM and cryo-SEM across the range of concentrations and phase regimes could be a powerful method for investigating other systems of nanocylinders and rodlike molecules such as boron nitride nanotubes, silicon nanowires,⁴⁷ gold⁴⁸ and silver⁴⁹ nanorods, actin,⁵⁰ and cellulose⁵¹ and may permit the direct imaging of other phases (e.g., smectic,^{52,53} cholesteric,⁵⁴ and columnar⁵⁵) that so far have been elusive for CNT researchers.

ASSOCIATED CONTENT

Supporting Information

The Supporting Information is available free of charge on the ACS Publications website at DOI: 10.1021/acs.langmuir.7b00206.

Equatorial and azimuthal plots of the wide-angle X-ray two-dimensional diffraction of CNT fibers. (PDF)

AUTHOR INFORMATION

Corresponding Authors

*E-mail (M.P.): mp@rice.edu.

*E-mail (Y.T.): ishi@tx.technion.ac.il.

ORCID

Olga Kleinerman: 0000-0001-7139-0999

Author Contributions

[§]These authors contributed equally.

Notes

The authors declare no competing financial interest.

ACKNOWLEDGMENTS

We thank Dr. Ellina Kesselman for excellent technical support and Dr. Rafail Khalfin for the X-ray experiments. This work was supported by United States-Israel Binational Science Foundation (BSF) grant 2012223, Welch Foundation grant C-1668, Air Force Office of Scientific Research grants FA9550-09-1-0590 and FA9550-15-1-0370, MURI grant FA9550-12-1-0035, and Teijin Aramid BV. Cryo-TEM and cryo-SEM imaging were performed at the Technion Laboratory for Electron Microscopy of Soft Materials, supported by the Technion Russell Berrie Nanotechnology Institute (RBNI).

REFERENCES

- (1) Saito, R.; Dresselhaus, G.; Dresselhaus, M. *Physical Properties of Carbon Nanotubes*; Imperial College Press, 1998; pp 35–37.
- (2) Green, M. J.; Behabtu, N.; Pasquali, M.; Adams, W. W. Nanotubes as Polymers. *Polymer* **2009**, *50*, 4979–4997.
- (3) Shaffer, M. S. P.; Windle, A. H. Analogies between Polymer Solutions and Carbon Nanotube Dispersions. *Macromolecules* **1999**, *32*, 6864–6866.
- (4) Green, M. J. Analysis and Measurement of Carbon Nanotube Dispersions: Nanodispersion versus Macrodissolution. *Polym. Int.* **2010**, *59*, 1319–1322.
- (5) Bahr, J. L.; Mickelson, E. T.; Bronikowski, M. J.; Smalley, R. E.; Tour, J. M. Dissolution of Small Diameter Single-Wall Carbon Nanotubes in Organic Solvents? *Chem. Commun.* **2001**, 363, 193–194.
- (6) Ramesh, S.; Ericson, L. M.; Davis, V. A.; Saini, R. K.; Kittrell, C.; Pasquali, M.; Billups, W. E.; Adams, W. W.; Hauge, R. H.; Smalley, R. E. Dissolution of Pristine Single Walled Carbon Nanotubes in Supercacids by Direct Protonation. *J. Phys. Chem. B* **2004**, *108*, 8794–8798.
- (7) Davis, V. A.; Ericson, L. M.; Parra-Vasquez, A. N. G.; Fan, H.; Wang, Y.; Prieto, V.; Longoria, J. a.; Ramesh, S.; Saini, R. K.; Kittrell, C.; Billups, W. E.; Adams, W. W.; Hauge, R. H.; Smalley, R. E.; Pasquali, M. Phase Behavior and Rheology of SWNTs in Supercacids. *Macromolecules* **2004**, *37*, 154–160.
- (8) Davis, V. A.; Parra-Vasquez, A. N. G.; Green, M. J.; Rai, P. K.; Behabtu, N.; Prieto, V.; Booker, R. D.; Schmidt, J.; Kesselman, E.; Zhou, W.; Fan, H.; Adams, W. W.; Hauge, R. H.; Fischer, J. E.; Cohen, Y.; Talmon, Y.; Smalley, R. E.; Pasquali, M. True Solutions of Single-Walled Carbon Nanotubes for Assembly into Macroscopic Materials. *Nat. Nanotechnol.* **2009**, *4*, 830–834.
- (9) Duque, J. G.; Parra-Vasquez, A. N. G.; Behabtu, N.; Green, M. J.; Higginbotham, A. L.; Price, B. K.; Leonard, A. D.; Schmidt, H. K.; Lounis, B.; Tour, J. M.; Doorn, S. K.; Cognet, L.; Pasquali, M.

Diameter-Dependent Solubility of Single-Walled Carbon Nanotubes. *ACS Nano* **2010**, *4*, 3063–3072.

(10) Parra-Vasquez, A. N. G.; Behabtu, N.; Green, M. J.; Pint, C. L.; Young, C. C.; Schmidt, J.; Kesselman, E.; Goyal, A.; Ajayan, P. M.; Cohen, Y.; Talmon, Y.; Hauge, R. H.; Pasquali, M. Spontaneous Dissolution of Ultralong Single- and Multiwalled Carbon Nanotubes. *ACS Nano* **2010**, *4*, 3969–3978.

(11) Green, M. J.; Parra-Vasquez, A. N. G.; Behabtu, N.; Pasquali, M. Modeling the Phase Behavior of Polydisperse Rigid Rods with Attractive Interactions with Applications to Single-Walled Carbon Nanotubes in Superacids. *J. Chem. Phys.* **2009**, *131*, 084901.

(12) Behabtu, N.; Young, C. C.; Tsentalovich, D. E.; Kleiner, O.; Wang, X.; Ma, A. W. K.; Bengio, E. A.; ter Waarbeek, R. F.; de Jong, J. J.; Hoogerwerf, R. E.; Fairchild, S. B.; Ferguson, J. B.; Maruyama, B.; Kono, J.; Talmon, Y.; Cohen, Y.; Otto, M. J.; Pasquali, M. Strong, Light, Multifunctional Fibers of Carbon Nanotubes with Ultrahigh Conductivity. *Science* **2013**, *339*, 182–186.

(13) Ericson, L. M.; Fan, H.; Peng, H.; Davis, V. A.; Zhou, W.; Sulpizio, J.; Wang, Y.; Booker, R.; Vavro, J.; Guthy, C.; Parra-Vasquez, A. N. G.; Kim, M. J.; Ramesh, S.; Saini, R. K.; Kittrell, C.; Lavin, G.; Schmidt, H.; Adams, W. W.; Billups, W. E.; Pasquali, M.; Hwang, W. F.; Hauge, R. H.; Fischer, J. E.; Smalley, R. E. Macroscopic, Neat, Single-Walled Carbon Nanotube Fibers. *Science* **2004**, *305*, 1447–1450.

(14) Kwolek, S. L.; Morgan, P. W.; Schaefgen, J. R.; Gulrich, L. W. Synthesis, Anisotropic Solutions, and Fibers of Poly(1,4-Benzamide). *Macromolecules* **1977**, *10*, 1390–1396.

(15) Tanner, D.; Fitzgerald, J. A.; Phillips, B. R. The Kevlar Story - an Advanced Materials Case Study. *Angew. Chem., Int. Ed. Engl.* **1989**, *28*, 649–654.

(16) Davis, V. A. Liquid Crystalline Assembly of Nanocylinders. *J. Mater. Res.* **2011**, *26*, 140–153.

(17) Miller, J. B.; Hobbie, E. K. Nanoparticles as Macromolecules. *J. Polym. Sci., Part B: Polym. Phys.* **2013**, *51*, 1195–1208.

(18) Bengio, E. A.; Tsentalovich, D. E.; Behabtu, N.; Kleiner, O.; Kesselman, E.; Schmidt, J.; Talmon, Y.; Pasquali, M. Statistical Length Measurement Method by Direct Imaging of Carbon Nanotubes. *ACS Appl. Mater. Interfaces* **2014**, *6*, 6139–6146.

(19) Tsentalovich, D. E.; Ma, A. W. K.; Lee, J. A.; Behabtu, N.; Bengio, E. A.; Choi, A.; Hao, J.; Luo, Y.; Headrick, R. J.; Green, M. J.; Talmon, Y.; Pasquali, M. Relationship of Extensional Viscosity and Liquid Crystalline Transition to Length Distribution in Carbon Nanotube Solutions. *Macromolecules* **2016**, *49*, 681–689.

(20) Parra-Vasquez, A. N. G.; Stepanek, I.; Davis, V. A.; Moore, V. C.; Haroz, E. H.; Shaver, J.; Hauge, R. H.; Smalley, R. E.; Pasquali, M. Simple Length Determination of Single-Walled Carbon Nanotubes by Viscosity Measurements in Dilute Suspensions. *Macromolecules* **2007**, *40*, 4043–4047.

(21) Fakhri, N.; Tsybolski, D. A.; Cognet, L.; Weisman, R. B.; Pasquali, M. Diameter-Dependent Bending Dynamics of Single-Walled Carbon Nanotubes in Liquids. *Proc. Natl. Acad. Sci. U. S. A.* **2009**, *106*, 14219–14223.

(22) Zhou, W.; Fischer, J. E.; Heiney, P. A.; Fan, H.; Davis, V. A.; Pasquali, M.; Smalley, R. E. Single-Walled Carbon Nanotubes in Superacid: X-Ray and Calorimetric Evidence for Partly Ordered H₂SO₄. *Phys. Rev. B: Condens. Matter Mater. Phys.* **2005**, *72*, 045440.

(23) Zhou, W.; Heiney, P. A.; Fan, H.; Smalley, R. E.; Fischer, J. E. Single-Walled Carbon Nanotube-Templated Crystallization of H₂SO₄: Direct Evidence for Protonation. *J. Am. Chem. Soc.* **2005**, *127*, 1640–1641.

(24) Zakri, C. Carbon Nanotubes and Liquid Crystalline Phases. *Liq. Cryst. Today* **2007**, *16*, 1–11.

(25) Behabtu, N.; Green, M.; Pasquali, M. Carbon Nanotube-Based Neat Fibers. *Nano Today* **2008**, *3*, 24–34.

(26) Zakri, C.; Blanc, C.; Grelet, E.; Zamora-Ledezma, C.; Puech, N.; Anglaret, E.; Poulin, P. Liquid Crystals of Carbon Nanotubes and Graphene. *Philos. Trans. R. Soc., A* **2013**, *371*, 20120499.

(27) Tohyama, K.; Miller, W. G. Network Structure in Gels of Rod-like Polypeptides. *Nature* **1981**, *289*, 813–814.

(28) Bandyopadhyaya, R.; Nativ-Roth, E.; Regev, O.; Yerushalmi-Rozen, R. Stabilization of Individual Carbon Nanotubes in Aqueous Solutions. *Nano Lett.* **2002**, *2*, 25–28.

(29) Dror, Y.; Salalha, W.; Khalfin, R. L.; Cohen, Y.; Yarin, A. L.; Zussman, E. Carbon Nanotubes Embedded in Oriented Polymer Nanofibers by Electrospinning. *Langmuir* **2003**, *19*, 7012–7020.

(30) Moore, V. C.; Strano, M. S.; Haroz, E. H.; Hauge, R. H.; Smalley, R. E.; Schmidt, J.; Talmon, Y. Individually Suspended Single-Walled Carbon Nanotubes in Various Surfactants. *Nano Lett.* **2003**, *3*, 1379–1382.

(31) Kleiner, O.; Parra-Vasquez, A. N. G.; Green, M. J.; Behabtu, N.; Schmidt, J.; Kesselman, E.; Young, C. C.; Cohen, Y.; Pasquali, M.; Talmon, Y. Cryogenic-Temperature Electron Microscopy Direct Imaging of Carbon Nanotubes and Graphene Solutions in Superacids. *J. Microsc.* **2015**, *259*, 16–25.

(32) Onsager, L. The Effects of Shape on the Interaction of Colloidal Particles. *Ann. N. Y. Acad. Sci.* **1949**, *51*, 627–659.

(33) Flory, P. J. Phase Equilibria in Solutions of Rod-like Particles. *Proc. R. Soc. London, Ser. A* **1956**, *234*, 73–89.

(34) Behabtu, N. *Dissolution, Processing and Fluid Structure of Graphene and Carbon Nanotube in Superacids: The Route toward High Performance Multifunctional Materials*. Ph.D. Thesis, Rice University, 2012.

(35) Doi, M.; Edwards, S. F. The Theory of Polymer Dynamics. *The Theory of Polymer Dynamics*; Oxford University Press: Oxford, 1986; pp 324–348.

(36) Viamontes, J.; Oakes, P. W.; Tang, J. X. Isotropic to Nematic Liquid Crystalline Phase Transition of F-Actin Varies from Continuous to First Order. *Phys. Rev. Lett.* **2006**, *97*, 118103.

(37) Viamontes, J.; Tang, J. X. Continuous Isotropic-Nematic Liquid Crystalline Transition of F-Actin Solutions. *Phys. Rev. E: Stat. Phys., Plasmas, Fluids, Relat. Interdiscip. Top.* **2003**, *67*, 040701.

(38) Zhang, S.; Kinloch, I. A.; Windle, A. H. Mesogenicity Drives Fractionation in Lyotropic Aqueous Suspensions of Multiwall Carbon Nanotubes. *Nano Lett.* **2006**, *6*, 568–572.

(39) Jamali, V.; Behabtu, N.; Senyuk, B.; Lee, J. A.; Smalyukh, I. I.; van der Schoot, P.; Pasquali, M. Experimental Realization of Crossover in Shape and Director Field of Nematic Tactoids. *Phys. Rev. E* **2015**, *91*, 042507.

(40) Prinsen, P.; van der Schoot, P. Continuous Director-Field Transformation of Nematic Tactoids. *Eur. Phys. J. E: Soft Matter Biol. Phys.* **2004**, *13*, 35–41.

(41) Everts, J. C.; Punter, M. T. J. J. M.; Samin, S.; van der Schoot, P.; van Roij, R. A. Landau-de Gennes Theory for Hard Colloidal Rods: Defects and Tactoids. *J. Chem. Phys.* **2016**, *144*, 194901.

(42) Mirri, F.; Ma, A. W. K.; Hsu, T. T.; Behabtu, N.; Eichmann, S. L.; Young, C. C.; Tsentalovich, D. E.; Pasquali, M. High-Performance Carbon Nanotube Transparent Conductive Films by Scalable Dip Coating. *ACS Nano* **2012**, *6*, 9737–9744.

(43) Abe, A.; Flory, P. J. Statistical Thermodynamics of Mixtures of Rodlike Particles in Ternary Systems. *Macromolecules* **1978**, *11*, 1122–1126.

(44) Wensink, H. H.; Vroege, G. J. Isotropic–nematic Phase Behavior of Length-Polydisperse Hard Rods. *J. Chem. Phys.* **2003**, *119*, 6868.

(45) Speranza, A.; Sollich, P. Isotropic-Nematic Phase Equilibria in the Onsager Theory of Hard Rods with Length Polydispersity. *Phys. Rev. E: Stat. Phys., Plasmas, Fluids, Relat. Interdiscip. Top.* **2003**, *67*, 061702.

(46) Kleiner, O. *A Nanostructural Study of Carbon Nanotubes in Superacids: Isotropic Solutions, Liquid Crystalline Phase, and Spun Fibers*. Master's Thesis, Technion-Israel Institute of Technology, Faculty of Chemical Engineering, 2013.

(47) He, J. Z.; Xu, J. B.; Xu, M. S.; Xie, Z.; Wilson, I. H.; Ma, X. L.; Li, Q.; Wang, N.; Hung, L. S.; Lee, C. S.; Lee, S. T. Dispersion, Refinement, and Manipulation of Single Silicon Nanowires. *Appl. Phys. Lett.* **2002**, *80*, 1812–1814.

- (48) van der Zande, B. M. I.; Böhmer, M. R.; Fokkink, L. G. J.; Schönenberger, C. Colloidal Dispersions of Gold Rods: Synthesis and Optical Properties. *Langmuir* **2000**, *16*, 451–458.
- (49) Pietrobon, B.; McEachran, M.; Kitaev, V. Synthesis of Size-Controlled Faceted Pentagonal Silver Nanorods with Tunable Plasmonic Properties and Self-Assembly of These Nanorods. *ACS Nano* **2009**, *3*, 21–26.
- (50) Wong, G. C. L. Hierarchical Self-Assembly of F-Actin and Cationic Lipid Complexes: Stacked Three-Layer Tubule Networks. *Science* **2000**, *288*, 2035–2039.
- (51) Habibi, Y.; Lucia, L. A.; Rojas, O. J. Cellulose Nanocrystals: Chemistry, Self-Assembly, and Applications. *Chem. Rev.* **2010**, *110*, 3479–3500.
- (52) Chen, J. T.; Thomas, E. L.; Ober, C. K.; Mao, G. P. Self-Assembled Smectic Phases in Rod-Coil Block Copolymers. *Science* **1996**, *273*, 343–346.
- (53) Somoza, A. M.; Sagui, C.; Roland, C. Liquid-Crystal Phases of Capped Carbon Nanotubes. *Phys. Rev. B: Condens. Matter Mater. Phys.* **2001**, *63*, 81403.
- (54) Ao, G.; Nepal, D.; Davis, V. A. Rheology of Lyotropic Cholesteric Liquid Crystal Forming Single-Wall Carbon Nanotube Dispersions Stabilized by Double-Stranded DNA. *Rheol. Acta* **2016**, *55*, 717–725.
- (55) Zhang, S.; Kumar, S. Carbon Nanotubes as Liquid Crystals. *Small* **2008**, *4*, 1270–1283.